

CANCER

Visualization nanozyme based on tumor microenvironment “unlocking” for intensive combination therapy of breast cancer

Zhiyi Wang¹, Ziyuan Li¹, Zhaoli Sun^{1,2}, Shuren Wang¹, Zeeshan Ali¹, Sihao Zhu¹, Sha Liu¹, Qiushi Ren¹, Fugeng Sheng³, Baodui Wang⁴, Yanglong Hou^{1*}

Nanozymes as artificial enzymes that mimicked natural enzyme-like activities have received great attention in cancer therapy. However, it remains a great challenge to design nanozymes that precisely exert its activity in tumor without producing off-target toxicity to surrounding normal tissues. Here, we report a synergetic enhancement strategy through the combination between nanozyme and tumor vascular normalization to destruct tumors, which was based on tumor microenvironment (TME) “unlocking.” This nanozyme that we developed not only has photothermal properties but also can produce reactive oxygen species efficiently under the stimulation of TME. Moreover, this nanozyme also showed remarkable imaging performance in fluorescence imaging in the second near-infrared region and magnetic resonance imaging for visualization tracing in vivo. The process of combination therapy showed remarkable therapeutic effect for breast cancer. This study provides a therapeutic strategy by the cooperation between multifunctional nanozyme and tumor vascular normalization for intensive combination therapy of breast cancer.

INTRODUCTION

Breast cancer is the most frequent malignancy in women worldwide and is a heterogeneous disease on the molecular level (1). The heterogeneity of breast cancer tissue usually makes it easy to cause multidrug resistance of tumor, tumor recurrence, or metastasis, which leads to the decline of therapeutic effect (2). The principal reason is that there are differences from genotype to phenotype in the same tumor, resulting in different sensitivity, growth speed, invasion ability, prognosis, and other aspects of tumor cells to drugs (3–5). A more accurate combination therapy based on tumor heterogeneity could give full play to the maximum effect, produce minimum side effects, and avoid the occurrence of multidrug resistance (6–8). Recently, combination therapy has been extremely advocated in clinical application. For instance, the simultaneous administration of two or multiple therapeutic agents would modulate different signaling pathways involved in the tumor progression (9, 10), bringing many advantages including synergetic responses, reduced drug resistance, and mitigatory side effects. Therefore, it is of great significance to develop a multimode tumor cooperative therapy system to improve the therapeutic effect of breast cancer.

In the early 1970s, as a young surgeon who frequently encountered cancer in patients, Judah Folkman observed that tumor tissue was enriched by an extraordinarily high number of blood vessels that were fragile and often hemorrhagic (11, 12). The angiogenesis translational research started at that time and has lasted for nearly 50 years. At present, the results show that blocking angiogenesis can retard tumor growth, but it may also increase metastasis paradoxically

(13, 14). This issue may be solved by vessel normalization, including increasing pericyte coverage, improving tumor vessel perfusion, reducing the permeability of blood vessels, and mitigating hypoxia consequently (15). Therefore, the normalization of tumor blood vessels is closely related to the regulation of tumor microenvironment (TME). Both humanized monoclonal antibody bevacizumab as the first anti-vascular endothelial growth factor (VEGF) agents and plasmid expressing interfering RNA targeting VEGF (shVEGF) have been used in cancer therapy (16). In 2017, Zhang elucidated an unexpected role of T helper 1 (T_H1) cells in vasculature and immune reprogramming. This finding confirmed that tumor blood vessels and immune system can affect each other's functions and proposed that T_H1 cells may be a marker and a determinant of both immune checkpoint blockade and anti-angiogenesis efficacy (15). Thus, the combined therapy with tumor vessel normalization is expected to improve the therapeutic effect of breast cancer.

Since Gao *et al.* (17) reported the first evidence of Fe₃O₄ nanoparticles (NPs) as peroxidase mimetics in 2007, various nanomaterials have been identified that have intrinsic enzyme-like activities (18, 19). Because of the similar enzymatic kinetics and mechanisms of natural enzymes under physiological conditions, this kind of nanomaterials is called “nanozyme” (20). The past decade have witnessed the rapid development of nanozymes in biomedical applications including immunoassays, biosensors, antibacterial, and antibiofilm agents (21, 22). Tailored to the specific TME, including the excessive production of acid and hydrogen peroxide, the introduction of highly active nanozyme, through Fenton and Fenton-like reactions to produce reactive oxygen species (ROS), has been used in the chemodynamic therapy (CDT) of cancer (23). A great challenge for in vivo application of nanozyme is the precise control of the selective execution of the desired activity because off-target activity will lead to unpredictable side effects. For instance, Fe₃O₄ NPs have peroxidase-like activity to increase reactive ROS under acidic pH. However, these NPs exhibit catalase-like activity in neutral condition, which will lead to removal of ROS (24). In the process of ROS-related treatment, the former is beneficial to improve the therapeutic effect, while the latter should be

Copyright © 2020
The Authors, some
rights reserved;
exclusive licensee
American Association
for the Advancement
of Science. No claim to
original U.S. Government
Works. Distributed
under a Creative
Commons Attribution
NonCommercial
License 4.0 (CC BY-NC).

¹Beijing Key Laboratory for Magnetoelectric Materials and Devices, Department of Materials Science and Engineering, College of Engineering, Beijing Innovation Centre for Engineering Science and Advanced Technology, Peking University, Beijing 100871, China. ²College of Life Science, Peking University, Beijing 100871, China. ³Fifth Medical Center of Chinese PLA General Hospital, Beijing 100071, China. ⁴State Key Laboratory of Applied Organic Chemistry, Key Laboratory of Nonferrous Metal Chemistry and Resources Utilization of Gansu Province, Lanzhou University, Lanzhou 730000, China.

*Corresponding author. Email: hou@pku.edu.cn

inhibited. Therefore, it is necessary to design a strategy to coordinate the activity of nanozyme through the regulation of TME for optimal functioning upon entering of the nanozyme into its target cell.

As a proof of concept, we have constructed a previously unknown strategy to regulate TME by tumor vessel normalization to optimize the anticancer effect of visualization nanozyme. Primarily, monodisperse core-shell $\text{Ag}_2\text{S}@Fe_2\text{C}$ heterogeneous NPs were synthesized by seeded growth-based thermal decomposition method in organic phase. Afterward, to improve the tumor targeting, we designed a precise targeting NP-based nanozyme system ($\text{Ag}_2\text{S}@Fe_2\text{C}$ -DSPE-PEG-iRGD) by coating a tumor-homing penetration peptide-modified Distearoyl phosphoethanolamine-PEG-iRGD peptide (DSPE-PEG-iRGD) on the surface of $\text{Ag}_2\text{S}@Fe_2\text{C}$ NPs. This nanozyme showed remarkable intracellular uptake, good fluorescence performance, and up-regulation of ROS production in 4T1 cells. Furthermore, this nanozyme displayed high-resolution bioimaging effect in vivo in 4T1 breast cancer-bearing mice, which included fluorescence imaging in the second near-infrared region (NIR-II) and magnetic resonance imaging (MRI). Moreover, the improved therapeutic effect was observed by the treatment of $\text{Ag}_2\text{S}@Fe_2\text{C}$ -DSPE-PEG-iRGD after combination with the tumor vascular normalization based on bevacizumab during the treatment in 4T1 breast cancer-bearing mice. Our study provides a new therapeutic strategy by the cooperation between

catalysis of imaging-guided nanozyme and tumor vascular normalization for intensive combination therapy of breast cancer.

RESULTS

Synthesis and characterization

The scheme of the combination therapeutic strategy was shown in Fig. 1, including the schematic illustration of combination therapeutic strategy (Fig. 1A) and biochemical process for multifunctional $\text{Ag}_2\text{S}@Fe_2\text{C}$ -DSPE-PEG-iRGD in breast cancer cell (Fig. 1B). Subsequently, the schematic design of core-shell $\text{Ag}_2\text{S}@Fe_2\text{C}$ -DSPE-PEG-iRGD is presented in Fig. 2A. First, monodispersed $\text{Ag}_2\text{S}@Fe_2\text{C}$ NPs were synthesized by seed-mediated growth method with thermal decomposition in organic phase. The synthesis of $\text{Ag}_2\text{S}@Fe_2\text{C}$ NPs comprises two steps: (i) the preparation of Ag_2S quantum dots (QDs) (fig. S1) and (ii) the iron carbide coating on the surface of Ag_2S QDs to obtain $\text{Ag}_2\text{S}@Fe_2\text{C}$ NPs (Fig. 2B). Ag_2S QDs were prepared by thermal decomposition of a source precursor of Ag(DDTC) [$(\text{C}_2\text{H}_5)_2\text{NCS}_2\text{Ag}$]. (25). Fe_2C phase around Ag_2S QDs is regulated by ammonium bromide (NH_4Br), which has been reported in our previous studies (26, 27). Because the selective adsorption of Br ions weakened the bonding between Fe and C atoms, the process could promote the formation of low-carbon iron carbide

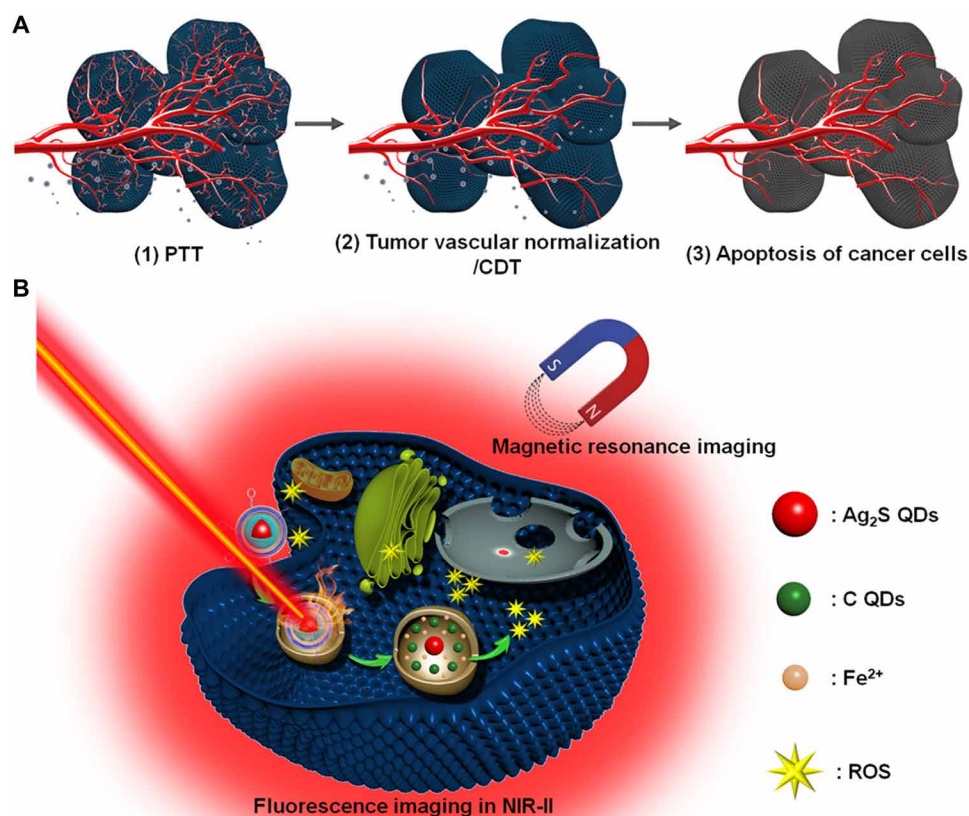


Fig. 1. Scheme of the combination therapeutic strategy between visualization nanozyme and tumor vascular normalization for breast cancer. (A) Schematic illustration of combination therapeutic strategy. (B) Schematic diagram of biochemical process for multifunctional $\text{Ag}_2\text{S}@Fe_2\text{C}$ -DSPE-PEG-iRGD in breast cancer cell. PTT, photothermal therapy.

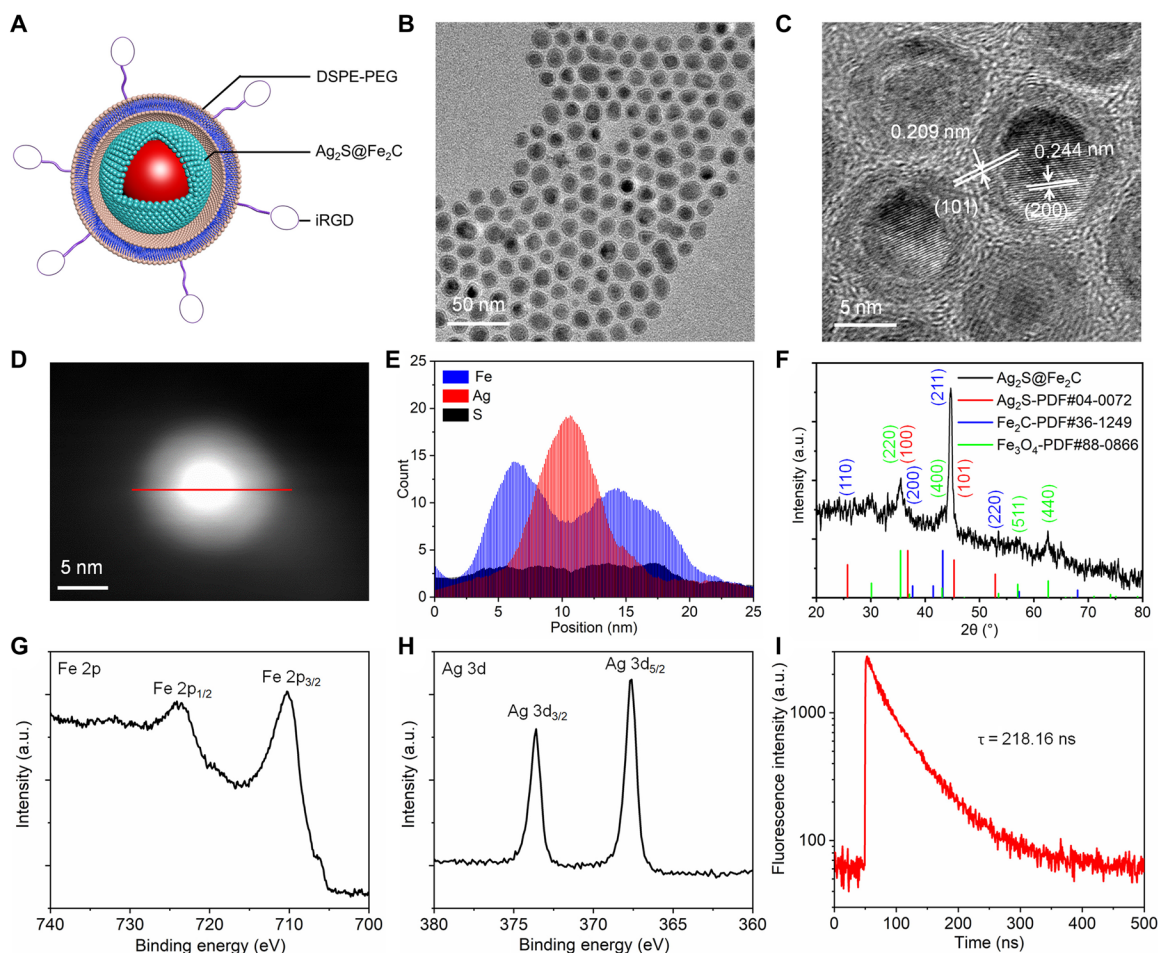


Fig. 2. Morphological and structural characterization. (A) Schematic illustration of the designed $\text{Ag}_2\text{S}@Fe_2\text{C}$ -DSPE-PEG-iRGD core-shell heterojunctions. (B) TEM image of $\text{Ag}_2\text{S}@Fe_2\text{C}$ NPs. (C) HRTEM image of $\text{Ag}_2\text{S}@Fe_2\text{C}$ NPs. (D and E) EDX line scan of $\text{Ag}_2\text{S}@Fe_2\text{C}$ NPs: Fe (blue), Ag (red), and S (black). (F) X-ray diffraction patterns of $\text{Ag}_2\text{S}@Fe_2\text{C}$ NPs. High-resolution XPS spectra of (G) Fe 2p and (H) Ag 3d obtained from $\text{Ag}_2\text{S}@Fe_2\text{C}$. (I) Lifetime decays of $\text{Ag}_2\text{S}@Fe_2\text{C}$ -DSPE-PEG-iRGD ($\lambda_{\text{excitation}} = 808$ nm). a.u., arbitrary units.

phase. Transmission electron microscope (TEM) images in Fig. 2B have shown that Ag_2S cores were semisurrounded by the Fe_2C domains with a thickness of ~ 3 nm. The high-resolution TEM (HRTEM) image depicted in Fig. 2C shows a lattice spacing between two (200) adjacent planes in Ag_2S of 0.244 nm and distance of 0.209 nm corresponding to the (101) planes of hexagonal Fe_2C . Furthermore, energy-dispersive x-ray (EDX) line scan of $\text{Ag}_2\text{S}@Fe_2\text{C}$ NPs was shown in Fig. 2 (D and E), which has confirmed the composition and core-shell structure of $\text{Ag}_2\text{S}@Fe_2\text{C}$ NPs. The results of x-ray diffraction (Fig. 2F) patterns were consistent with the characterization of TEM. However, the Fe_2C shell was protected from further oxidation by a ~ 1 -nm Fe_3O_4 shell with a spacing of 2.97 Å between the (220) planes of magnetite. The x-ray photoelectron spectroscopy (XPS) of Fe 2p (Fig. 2G and fig. S2) has confirmed the main existence of Fe^0 in $\text{Ag}_2\text{S}@Fe_2\text{C}$ NPs, and the weak satellite peaks are due to the local oxidation of NPs (26). The existence of Ag^+ was confirmed by the XPS of Ag 3d (Fig. 2H and fig. S2). DSPE-PEG-iRGD was synthesized by covalent bonding between DSPE-PEG-NHS (*N*-hydroxysuccinimide) and tumor-homing penetration peptide iRGD (CRGDKGPDC) subsequently (fig. S3) (28). $\text{Ag}_2\text{S}@Fe_2\text{C}$ -DSPE-PEG and $\text{Ag}_2\text{S}@Fe_2\text{C}$ -DSPE-PEG-iRGD were formulated

using water/oil (W/O) emulsion method (29). The formation of $\text{Ag}_2\text{S}@Fe_2\text{C}$ -DSPE-PEG-iRGD nanozyme was confirmed by the Fourier transform infrared spectrometer (fig. S4). The red shift of the absorption peak for the stretching vibration of the C=O from carboxyl group (1635 cm^{-1}) to amide bond (1689 cm^{-1}) proves the amination of DSPE-PEG-NHS and iRGD (fig. S4, i and iv). The existence of vibration absorption peaks (3410 and 1480 cm^{-1}) for N—H bond (fig. S4, iv) proved the obtaining of DSPE-PEG-iRGD. The hydrodynamic diameters of $\text{Ag}_2\text{S}@Fe_2\text{C}$ -DSPE-PEG-iRGD were 90.1 ± 20.3 nm (fig. S5A), and the zeta potential of $\text{Ag}_2\text{S}@Fe_2\text{C}$ -DSPE-PEG-iRGD was -12.2 mV (fig. S5B). The lifetime decays of $\text{Ag}_2\text{S}@Fe_2\text{C}$ -DSPE-PEG-iRGD ($\tau = 218.16$ ns, $\lambda_{\text{excitation}} = 808$ nm) were shown in Fig. 2I, which has proved that the NPs exhibit good luminescent property. The field-dependent magnetization curve of $\text{Ag}_2\text{S}@Fe_2\text{C}$ NPs and $\text{Ag}_2\text{S}@Fe_2\text{C}$ -DSPE-PEG-iRGD was measured at room temperature. After the modification of DSPE-PEG-iRGD, the magnetic saturation value is reduced from 116.97 to 50.12 electromagnetic unit (emu g^{-1}) (fig. S5C). This result proves that $\text{Ag}_2\text{S}@Fe_2\text{C}$ -DSPE-PEG-iRGD can be used as contrast agent in T_2 -MRI. Besides, better absorption capacity for light in the NIR was observed in $\text{Ag}_2\text{S}@Fe_2\text{C}$ -DSPE-PEG-iRGD compared to $\text{Ag}_2\text{S}@Fe_2\text{C}$ in fig. S5D.

Biodegradation and enzymatic activity of $\text{Ag}_2\text{S}@Fe_2\text{C}$ -DSPE-PEG nanozyme in vitro

The biodegradation performance of $\text{Ag}_2\text{S}@Fe_2\text{C}$ -DSPE-PEG was evaluated by time-dependent fluorescence spectra in 48 hours (Fig. 3A). With the prolongation of dispersion time of $\text{Ag}_2\text{S}@Fe_2\text{C}$ -DSPE-PEG in phosphate-buffered saline (PBS) buffer (pH 5.4). The fluorescence intensity increases with time at the emission wavelength of 410 nm, which has demonstrated that carbon QDs (C QDs) are produced during the degradation of $\text{Ag}_2\text{S}@Fe_2\text{C}$ -DSPE-PEG (30). The fluorescence spectra of $\text{Ag}_2\text{S}@Fe_2\text{C}$ -DSPE-PEG were dispersed in PBS buffer (pH 7.4), and PBS buffer (pH 5.4) after 7 days further confirmed the stability of pH-dependent $\text{Ag}_2\text{S}@Fe_2\text{C}$ -DSPE-PEG in fig. S6A. Subsequently, the evaluation of peroxidase-like activity of $\text{Ag}_2\text{S}@Fe_2\text{C}$ -DSPE-PEG with different pH values was shown in Fig. 3B and fig. S6B. The peroxidase-like activity increases with the decrease of pH value. Moreover, TEM images of the $\text{Ag}_2\text{S}@Fe_2\text{C}$ -DSPE-PEG after degradation in PBS with pH value of 5.4 in 48 hours was revealed in Fig. 3C. After 6 hours, the NPs maintain the integrity generally with only slight morphological changes (arrow indicated). After 24 hours, degradation occurred in most of NPs from morphology and size. In addition, the free state of Ag_2S QDs can be observed in the TEM image. After 48 hours, the mor-

phology of the NPs is completely disrupted and residues of the C QDs can be observed (arrow indicated). Since C QDs and graphene oxide (GO) have a similar structure, the fluorescence property can be determined by the π states of the sp^2 sites (31). Moreover, the samples that were obtained from $\text{Ag}_2\text{S}@Fe_2\text{C}$ NP degradation in HCl solution (1 M) before and after 12 hours (fig. S7A) were characterized by XPS (fig. S7B). Normalized high-resolution XPS spectra of C 1s proved the existence of low-valence carbon. Moreover, as shown in fig. S7C, the carbon K edge spectrum of samples collected above shows a clear sp^2 signal with energy loss peaks at 283 eV ($1s \rightarrow \pi^*$) and 293 eV ($1s \rightarrow \sigma^*$), which proved the existence of sp^2 -hybridized carbon in $\text{Ag}_2\text{S}@Fe_2\text{C}$ NPs (32). Therefore, we can infer that these sp^2 -hybridized carbons were obtained during the thermal decomposition synthesis of $\text{Ag}_2\text{S}@Fe_2\text{C}$ NPs. To further prove the above speculation, the biodegradation behavior and structural evolution of $\text{Ag}_2\text{S}@Fe_2\text{C}$ -DSPE-PEG were further evaluated in 4T1 cells. After 24 hours of intracellular coincubation, $\text{Ag}_2\text{S}@Fe_2\text{C}$ -DSPE-PEG was almost degraded into ultrasmall NPs. These results were exhibited in bio-TEM images in Fig. 3D.

On the basis of the above experimental results, Fig. 3E illustrated the degradation process of $\text{Ag}_2\text{S}@Fe_2\text{C}$ -DSPE-PEG. The external DSPE-PEG degraded gradually because of hydrolysis of the ester

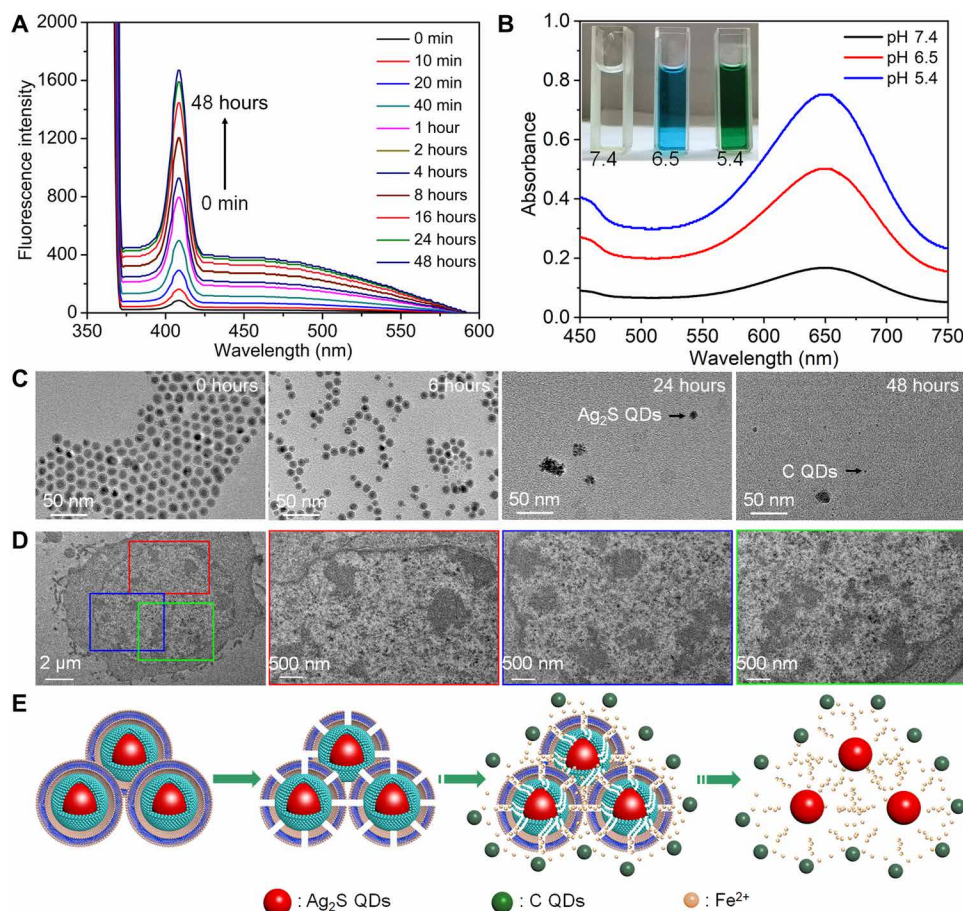


Fig. 3. Biodegradation performance. (A) Time-dependent fluorescence spectra of $\text{Ag}_2\text{S}@Fe_2\text{C}$ -DSPE-PEG dispersed in PBS buffer solution (pH 5.4, $\lambda_{\text{excitation}} = 370$ nm, $\lambda_{\text{em}} = 410$ nm). (B) Peroxidase-like activity of $\text{Ag}_2\text{S}@Fe_2\text{C}$ -DSPE-PEG with different pH values (5.4, 6.5, and 7.4). Photo credit: Zhiyi Wang, Peking University, China. (C) TEM images (scale bars, 50 nm) of the $\text{Ag}_2\text{S}@Fe_2\text{C}$ -DSPE-PEG after degradation in PBS (pH 5.4) for 0, 6, 24, and 48 hours. (D) Bio-TEM images (scale bar, 2 μm) of 4T1 cells incubated with $\text{Ag}_2\text{S}@Fe_2\text{C}$ -DSPE-PEG for 24 hours (scale bars, 500 nm) of different regions enlarged. (E) Schematic representation of the degradation process of the $\text{Ag}_2\text{S}@Fe_2\text{C}$ -DSPE-PEG in the physiological environment.

linkage into segments (reduced molecular weight), oligomers and monomers, and lastly carbon dioxide and water (33) after the $\text{Ag}_2\text{S}@Fe_2C$ -DSPE-PEG were dispersed in the physiological environment. Degradation of DSPE-PEG disrupts the NPs and triggers release of Fe^{2+} and C QDs from the Fe_2C shell, which degrades rapidly if it is not protected by DSPE-PEG. After the degradation of Fe_2C shell, Ag_2S QDs were commonly found in bio-TEM images. Because the C QDs and Ag_2S QDs are relatively stable in physiological environment, it is beneficial to be metabolized out of the body through the kidney and liver (34, 35). The unique biodegradability of the $\text{Ag}_2\text{S}@Fe_2C$ -DSPE-PEG not only circumvents rapid degradation of the optical performance but also enables harmless clearance from the body in a reasonable period after the end of therapeutic functions in vivo.

Evaluation of enhanced cellular uptake, ROS-generation, and 4T1 cell killing ability

The modification by DSPE-PEG-iRGD enhanced the biocompatibility of NPs under physiological conditions, which was proved by cell

counting kit-8 (CCK8) assay in fig. S8. The cellular uptake of $\text{Ag}_2\text{S}@Fe_2C$ -DSPE-PEG-iRGD in 4T1 cells was evaluated by multi-dimensional confocal microfluorescence imaging system in Fig. 4A ($\lambda_{\text{excitation}} = 808 \text{ nm}$). These results revealed that a minority of red fluorescence could be observed in 4T1 cells treated with $\text{Ag}_2\text{S}@Fe_2C$ -DSPE-PEG, indicating the limited cellular uptake. However, much stronger red fluorescence could be found after coinubation with $\text{Ag}_2\text{S}@Fe_2C$ -DSPE-PEG-iRGD, which is mainly located in cytoplasm, instead of nuclei [staining by 4',6-diamidino-2-phenylindole (DAPI), $\lambda_{\text{excitation}} = 405 \text{ nm}$]. These results suggested that the $\text{Ag}_2\text{S}@Fe_2C$ -DSPE-PEG-iRGD performed higher cellular uptake after the modification with tumor-homing penetration peptide iRGD.

Subsequently, we further evaluated the nanozyme activity of $\text{Ag}_2\text{S}@Fe_2C$ -DSPE-PEG-iRGD in cancer cells. Because nonfluorescent dihydrorhodamine 123 (DHR123) can be oxidized by ROS into green fluorescent rhodamine 123, DHR123 was used as an intracellular ROS indicator (36). Fortunately, the strongest fluorescence intensity was shown in the group of $\text{Ag}_2\text{S}@Fe_2C$ -DSPE-PEG-iRGD under the irradiation of 808-nm laser, which demonstrated that the nanozyme

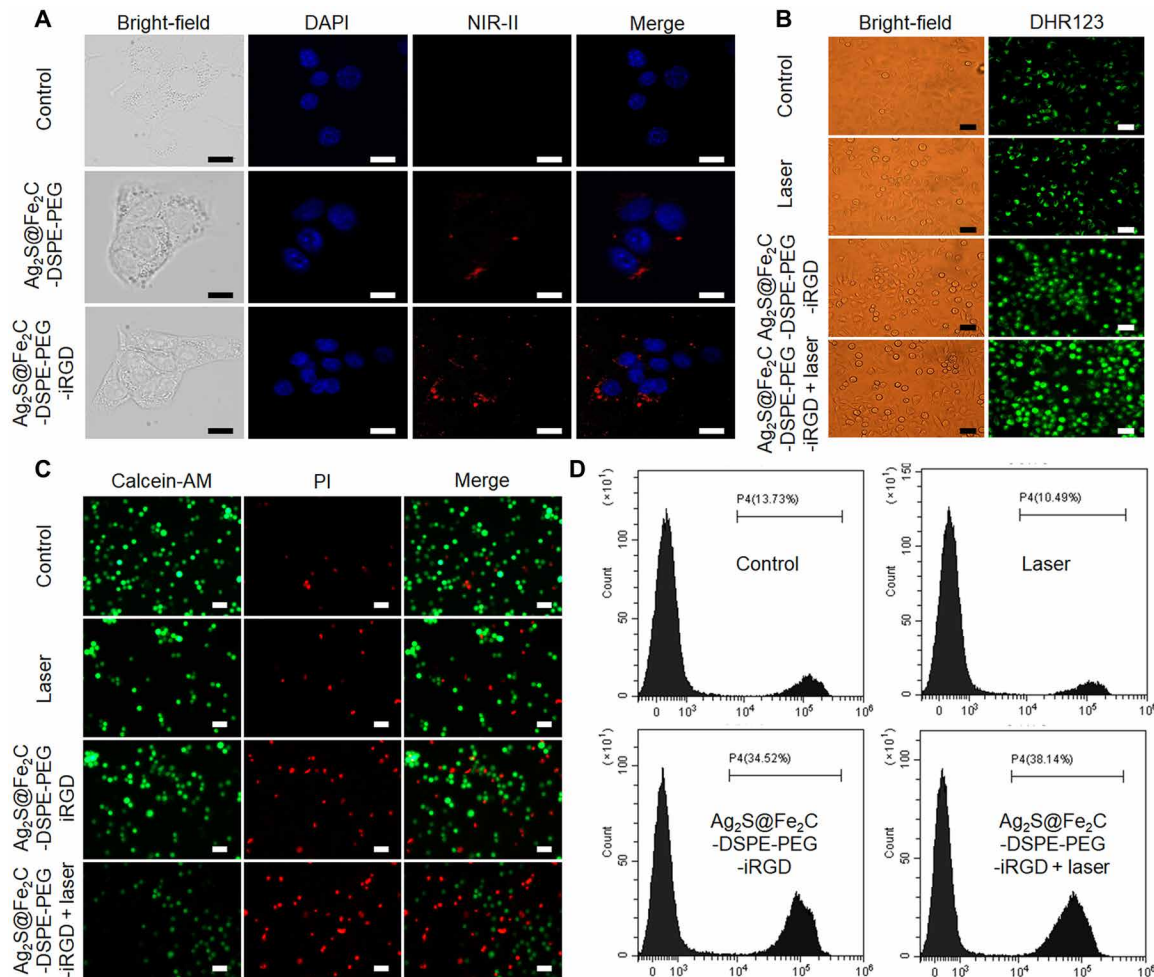


Fig. 4. Cell experiments. (A) Confocal laser scanning microscopy images (scale bars, 5 μm) of in 4T1 cells treated with saline, $\text{Ag}_2\text{S}@Fe_2C$ -DSPE-PEG, and $\text{Ag}_2\text{S}@Fe_2C$ -DSPE-PEG-iRGD in NIR-II. (B) Singlet oxygen generation evaluated by DHR123 in 4T1 cells treated with saline only, laser only, $\text{Ag}_2\text{S}@Fe_2C$ -DSPE-PEG, and $\text{Ag}_2\text{S}@Fe_2C$ -DSPE-PEG + laser (scale bars, 50 μm). (C) Fluorescence images (scale bars, 100 μm) of the 4T1 cells stained with calcein-AM (live cells, green fluorescence) and PI (dead cells, red fluorescence) after incubation with saline only, laser only, $\text{Ag}_2\text{S}@Fe_2C$ -DSPE-PEG, and $\text{Ag}_2\text{S}@Fe_2C$ -DSPE-PEG + laser. (D) Corresponding flow cytometry data of the 4T1 cells stained with PI (dead cells, red fluorescence) after incubation with saline only, laser only, $\text{Ag}_2\text{S}@Fe_2C$ -DSPE-PEG, and $\text{Ag}_2\text{S}@Fe_2C$ -DSPE-PEG + laser.

activity of $\text{Ag}_2\text{S}@Fe_2C\text{-DSPE-PEG-iRGD}$ was also enhanced compared with other groups (Fig. 4B). In the previous study, we reported the evaluation method of photothermal efficiency of nanomaterials (27, 37, 38). These results in fig. S11 demonstrated that $\text{Ag}_2\text{S}@Fe_2C\text{-DSPE-PEG-iRGD}$ is a highly efficient photothermal therapy agent. The 4T1 cell killing ability was evaluated in fluorescence micrographs in Fig. 4C [costained by calcein-AM and propidium iodide (PI)]. The group of $\text{Ag}_2\text{S}@Fe_2C\text{-DSPE-PEG-iRGD}$ under the irradiation of 808-nm laser showed the maximum range of dead cell markers, which proved that it has the strongest killing efficiency of 4T1 cells. Furthermore, corresponding flow cytometry data of the 4T1 cells stained with PI (dead cells, red fluorescence) was shown in Fig. 4D after incubation with saline only, the irradiation of 808-nm laser only, $\text{Ag}_2\text{S}@$

$Fe_2C\text{-DSPE-PEG-iRGD}$, and $\text{Ag}_2\text{S}@Fe_2C\text{-DSPE-PEG-iRGD}$ under the irradiation of 808-nm laser. These results are consistent with above.

Biodistribution imaging and biocompatible in vivo

The fluorescent emission spectrum of $\text{Ag}_2\text{S}@Fe_2C$ and $\text{Ag}_2\text{S}@Fe_2C\text{-DSPE-PEG-iRGD}$ in NIR-II was shown in Fig. 5A. Under the excitation of 808-nm laser, the fluorescent emission wavelength is 1071 nm. Subsequently, fluorescence imaging in NIR-II was carried out to track the in vivo behaviors of $\text{Ag}_2\text{S}@Fe_2C\text{-DSPE-PEG}$ and $\text{Ag}_2\text{S}@Fe_2C\text{-DSPE-PEG-iRGD}$ (20 mg kg^{-1} , 200 μ l) after intravenous injection into 4T1 breast cancer-bearing nude mice, with the excitation wavelength of 808 nm (Fig. 5B). The tumor site of $\text{Ag}_2\text{S}@Fe_2C\text{-DSPE-PEG-iRGD}$ group showed strong luminescence signals

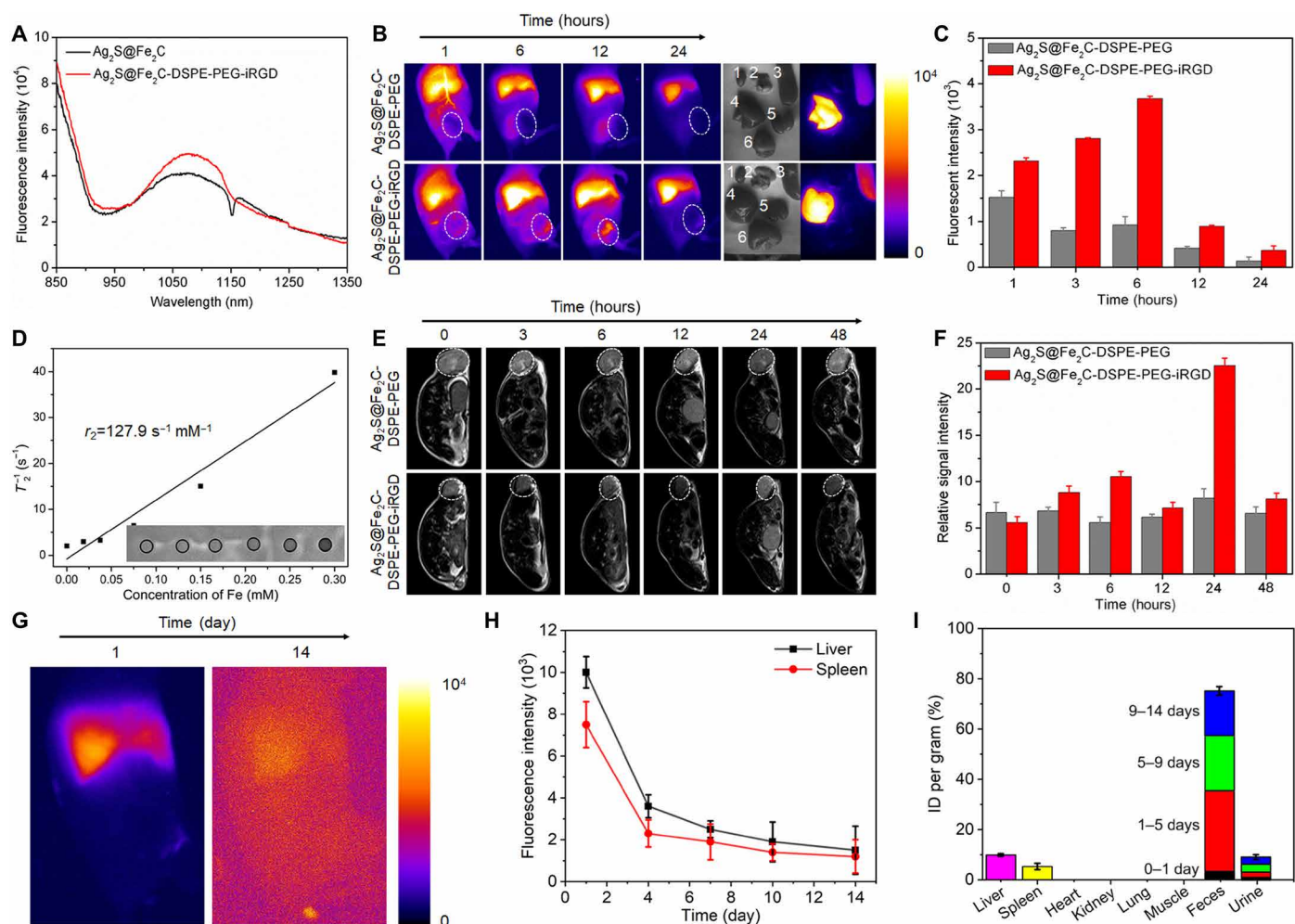


Fig. 5. In vivo imaging and evaluation of biocompatibility for rapid-excretable $\text{Ag}_2\text{S}@Fe_2C\text{-DSPE-PEG-iRGD}$. (A) The fluorescent emission spectrum of $\text{Ag}_2\text{S}@Fe_2C$ and $\text{Ag}_2\text{S}@Fe_2C\text{-DSPE-PEG-iRGD}$ in NIR-II under the excitation of 808-nm laser. (B) Real-time NIR-II fluorescence images of 4T1 breast cancer-bearing mice after intravenous injection of $\text{Ag}_2\text{S}@Fe_2C\text{-DSPE-PEG}$ and $\text{Ag}_2\text{S}@Fe_2C\text{-DSPE-PEG-iRGD}$. Ex vivo fluorescence images of heart (i), kidney (ii), spleen (iii), liver (iv), lung (v), and tumor (vi), which were obtained at 48 hours after injection. Photo credit: Zhiyi Wang, Peking University, China. (C) The fluorescence intensities of the tumor after intravenous injection of $\text{Ag}_2\text{S}@Fe_2C\text{-DSPE-PEG}$ and $\text{Ag}_2\text{S}@Fe_2C\text{-DSPE-PEG-iRGD}$, respectively. (D) T_2 relaxation rate ($1/T_2$) as a function of Fe concentration for the $\text{Ag}_2\text{S}@Fe_2C\text{-DSPE-PEG-iRGD}$. (E) Real-time MRI of 4T1 breast cancer-bearing mice after intravenous injection of $\text{Ag}_2\text{S}@Fe_2C\text{-DSPE-PEG}$ and $\text{Ag}_2\text{S}@Fe_2C\text{-DSPE-PEG-iRGD}$. (F) The relative MRI signal intensities changing at the tumor site after intravenous injection of $\text{Ag}_2\text{S}@Fe_2C\text{-DSPE-PEG}$ and $\text{Ag}_2\text{S}@Fe_2C\text{-DSPE-PEG-iRGD}$, respectively. (G) The wide-field images show the $\text{Ag}_2\text{S}@Fe_2C\text{-DSPE-PEG-iRGD}$ luminescence signals in liver and spleen at 1 and 14 days. (H) The excretion of $\text{Ag}_2\text{S}@Fe_2C\text{-DSPE-PEG-iRGD}$ from mouse liver and spleen can be seen by plotting the signal intensity in these organs (normalized to liver signal observed at 1 day) as a function of time over 2 weeks. (I) Biodistribution of $\text{Ag}_2\text{S}@Fe_2C\text{-DSPE-PEG-iRGD}$ in main organs and feces of $\text{Ag}_2\text{S}@Fe_2C\text{-DSPE-PEG-iRGD}$ -treated mice at 14 days. Error bars, means \pm SD ($n = 3$).

after 12 hours (Fig. 5C). In contrast, no obvious fluorescence signal appeared in the tumor site for $\text{Ag}_2\text{S}@Fe_2C$ -DSPE-PEG even after 24 hours. Moreover, the targeting capacity of $\text{Ag}_2\text{S}@Fe_2C$ -DSPE-PEG and $\text{Ag}_2\text{S}@Fe_2C$ -DSPE-PEG-iRGD was evaluated by ex vivo imaging of main organs (liver, spleen, lung, heart, and kidney) and tumors of mice after intravenous injection for 24 hours. Obvious fluorescence signals were clearly observed in the liver, tumor, and the main blood vessels near the tumor (Fig. 5B). The real-time movie of fluorescence imaging in NIR-II has been improved during the tail vein injection of $\text{Ag}_2\text{S}@Fe_2C$ -DSPE-PEG-iRGD (movie S1), which demonstrated that the nanozyme could achieve high-resolution microscopic imaging of blood vessels in mice, especially at the tumor site. These results reflect not only the advantages of fluorescence imaging in NIR-II with deeper tissue penetration but also the remarkable targeting effect of the $\text{Ag}_2\text{S}@Fe_2C$ -DSPE-PEG-iRGD for 4T1 breast cancer.

After calculation, the r_2 value of $\text{Ag}_2\text{S}@Fe_2C$ -DSPE-PEG was around $127.9 \text{ mM}^{-1} \text{ s}^{-1}$ when dispersed in water (Fig. 5D). Furthermore,

we assessed the T_2 -weighted MRI capability in vivo after intravenous injection of $\text{Ag}_2\text{S}@Fe_2C$ -DSPE-PEG and $\text{Ag}_2\text{S}@Fe_2C$ -DSPE-PEG-iRGD (20 mg kg^{-1} , $200 \mu\text{l}$) into 4T1 breast cancer-bearing nude mice. Figure 5E clearly indicates that the $\text{Ag}_2\text{S}@Fe_2C$ -DSPE-PEG-iRGD show stronger signal intensity and make the tumor darker than $\text{Ag}_2\text{S}@Fe_2C$ -DSPE-PEG after 24 hours of injection. These results suggest higher accumulations of $\text{Ag}_2\text{S}@Fe_2C$ -DSPE-PEG-iRGD at the tumor sites owing to the active targeting by tumor-homing penetration peptide iRGD. Therefore, $\text{Ag}_2\text{S}@Fe_2C$ NPs have the potential to be the agents for T_2 -weighted MRI.

The luminescence signal intensity in the main organs of mice, including liver and spleen, kept decreasing within the monitored time period of 14 days (Fig. 5, G and H). All the urine and feces excreted from mice were collected, and Ag was quantitatively detected by inductively coupled plasma optical emission spectrometry, revealing that $\sim 90\%$ of injected $\text{Ag}_2\text{S}@Fe_2C$ -DSPE-PEG-iRGD was excreted from the body in 14 days (Fig. 5I). This rapid, high-degree excretion could promote clinical translation of $\text{Ag}_2\text{S}@Fe_2C$ -DSPE-PEG-iRGD.

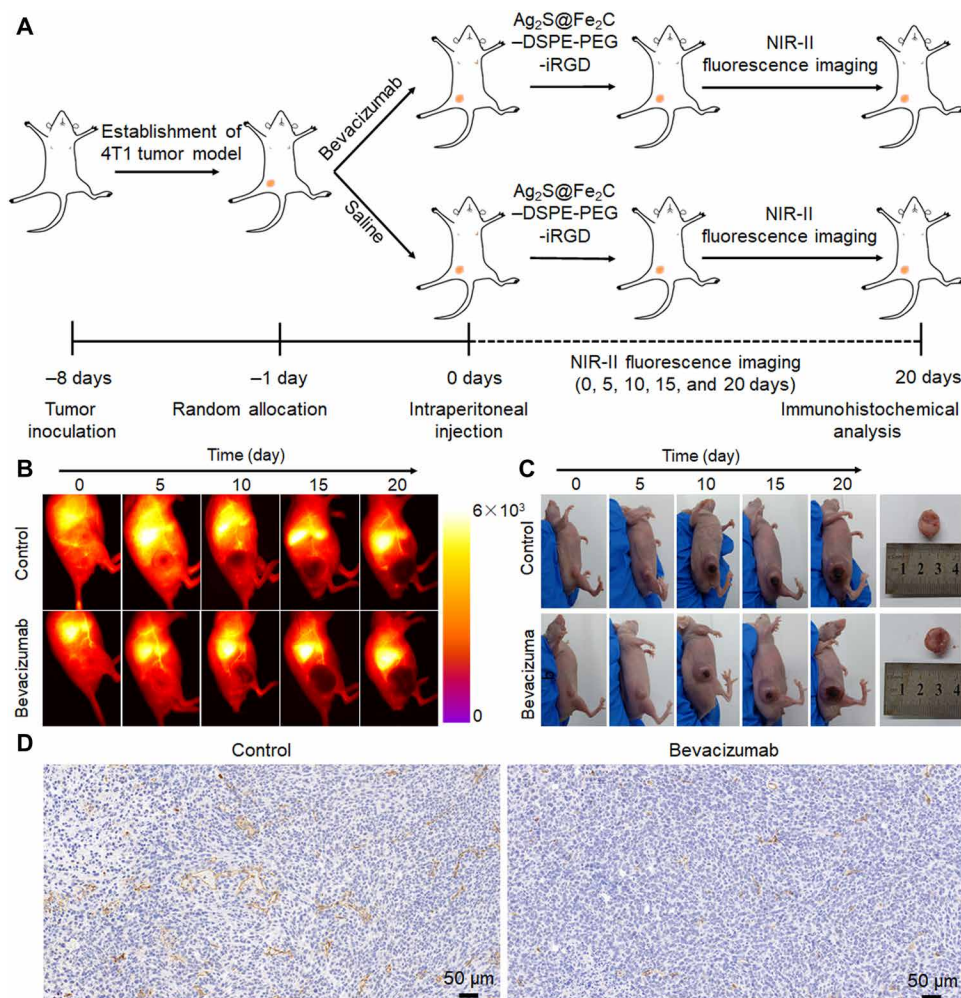


Fig. 6. Self-monitoring for inhibition of tumor angiogenesis. (A) Schematic illustration of self-monitoring for inhibition of tumor angiogenesis by $\text{Ag}_2\text{S}@Fe_2C$ -DSPE-PEG-iRGD after intraperitoneal injection of saline and bevacizumab. (B) Real-time NIR-II fluorescence images of 4T1 breast cancer-bearing mice after intraperitoneal injection of normal saline and bevacizumab by $\text{Ag}_2\text{S}@Fe_2C$ -DSPE-PEG-iRGD. (C) Representative photograph for volume change of tumor after intraperitoneal injection of normal saline and bevacizumab in 20 days. Inset: Corresponding harvested 4T1 breast cancer after 20 days. Photo credit: Zhiyi Wang, Peking University, China. (D) CD31 immunohistochemical staining of harvested 4T1 breast cancer after 20 days. Error bars, means \pm SD ($n = 5$).

Evaluation of tumor vascular normalization by bevacizumab

As mentioned before, angiogenesis as a physiologically complex process of proliferation and migration of endothelial cells could be suppressed by bevacizumab, which will benefit more for the tumor vascular normalization. We evaluated angiogenesis suppression effect of murine bevacizumab by fluorescence imaging in NIR-II and immunohistochemical analysis of CD31. Figure 6A showed the experimental diagram of 4T1 breast cancer angiogenesis by bevacizumab, which was imaged in NIR-II by intraperitoneal injection of low-dose $\text{Ag}_2\text{S}@\text{Fe}_2\text{C}$ -DSPE-PEG-iRGD in 4T1 breast cancer-bearing mice. Comparing to the group of saline injection, tumor angiogenesis inhibition effect by bevacizumab was demonstrated in the tumor site in the first 10 days (Fig. 6, B and C, and fig. S10). Then, tumor grew rapidly. Furthermore, the real-time movie of flu-

orescence imaging in NIR-II was provided in 0 and 20 days for each group (movies S2 to S5). These results also proved that bevacizumab cannot be used as a single drug for tumor. Moreover, CD31 immunohistochemical staining of harvested 4T1 tumor after 20 days was shown in Fig. 6D. We can clearly observe that the tumor vascular density in bevacizumab injection group is notably less than the control group, which is consistent with fluorescence imaging results. Therefore, bevacizumab could influence the tumor vascular normalization of 4T1 breast cancer.

In vivo cancer therapy and biosafety evaluation

Combination therapy (i.e., photothermal therapy, CDT, and tumor vascular normalization) was investigated by treatment of 4T1 breast cancer-bearing mice in vivo. Figure 7A showed the schematic

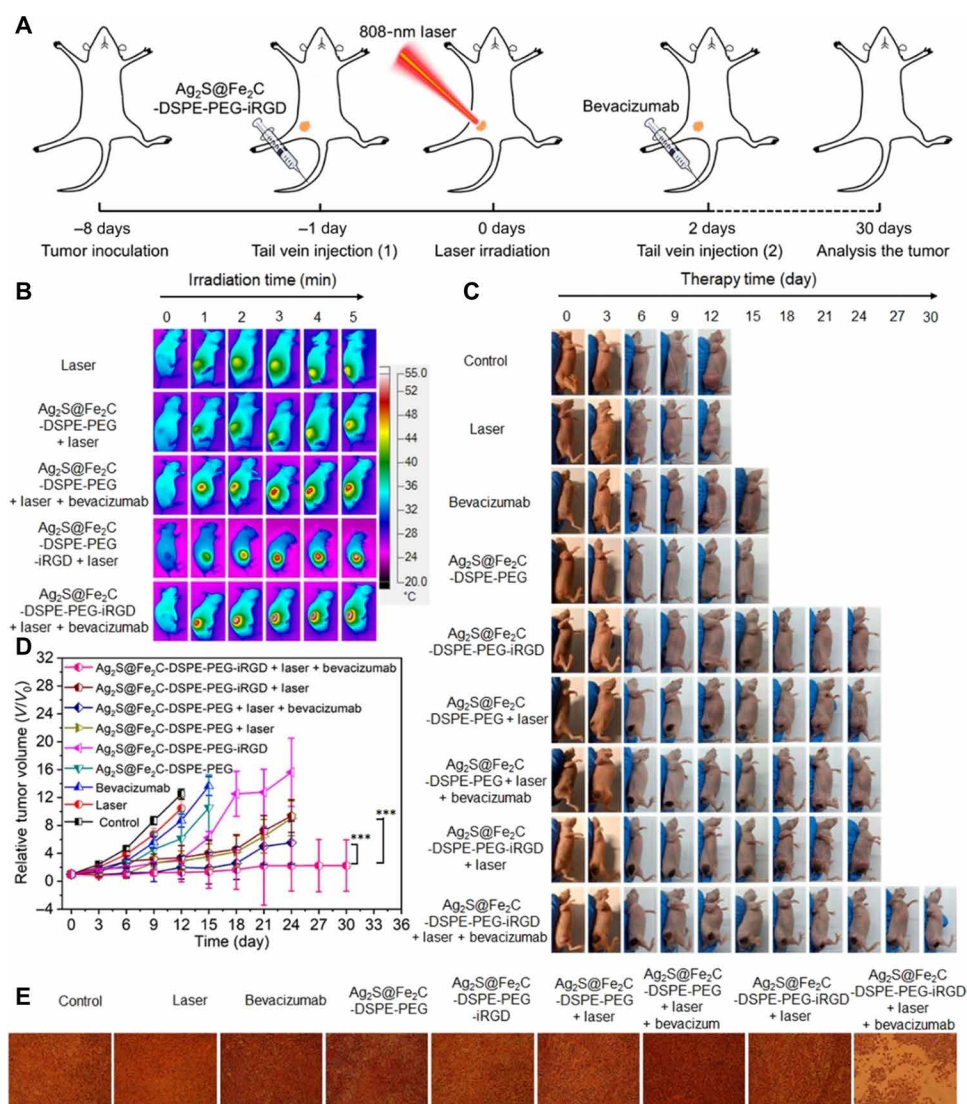


Fig. 7. Evaluation of combination therapy effect. (A) Schematic illustration of $\text{Ag}_2\text{S}@Fe_2C$ -DSPE-PEG-iRGD nanocapsule-based tumor therapy. (B) Real-time thermal infrared images of 4T1 breast cancer-bearing mice after intravenous injection of saline, $\text{Ag}_2\text{S}@Fe_2C$ -DSPE-PEG + laser, $\text{Ag}_2\text{S}@Fe_2C$ -DSPE-PEG + laser + bevacizumab, $\text{Ag}_2\text{S}@Fe_2C$ -DSPE-PEG-iRGD + laser, and $\text{Ag}_2\text{S}@Fe_2C$ -DSPE-PEG-iRGD + laser + bevacizumab under 808-nm laser irradiation (0.3 W cm^{-2} , 5 min). (C) Representative photograph for volume change of tumor in the different treatments in 30 days. Photo credit: Zhiyi Wang, Peking University, China. (D) Volume change of tumor in the different treatments. (E) H&E-stained images of tumor regions with different treatments. Error bars, means \pm SD ($n = 5$), unpaired *t* test.

illustration of the therapy process. When laser irradiation is applied to $\text{Ag}_2\text{S}@Fe_2C\text{-DSPE-PEG-iRGD}$ -injected mice, the local temperature of the tumor site rapidly increases from 37° to 54.7°C within 5 min, but for the mice treated with $\text{Ag}_2\text{S}@Fe_2C\text{-DSPE-PEG}$, the temperature only reaches to 46.8°C (Fig. 7B and fig. S10A). These results confirmed the superior targeting capability of $\text{Ag}_2\text{S}@Fe_2C\text{-DSPE-PEG-iRGD}$, which is consistent with the above results of bioimaging. Furthermore, the biodistribution of Ag after intravenous injection for 3 days was detected by inductively coupled plasma mass spectrometry, which confirmed the targeting capacity of $\text{Ag}_2\text{S}@Fe_2C\text{-DSPE-PEG-iRGD}$ in vivo (fig. S10B). Comparing with other groups, the remarkable antitumor efficiency of $\text{Ag}_2\text{S}@Fe_2C\text{-DSPE-PEG-iRGD}$ was demonstrated by tumor volume with significant inhibition and elimination in vivo (Fig. 7, C and D, and fig. S10C). The growth status of representative nude mice in each group at the time interval of 0, 3, 6, 9, 12, 15, 18, 21, 24, 27, and 30 days throughout the treatment period was observed (Fig. 7C and fig. S10D). The tumor of harvested mice injected with $\text{Ag}_2\text{S}@Fe_2C\text{-DSPE-PEG-iRGD}$ and bevacizumab under the laser irradiation (808 nm, 0.3 W cm⁻²) was completely eradicated after treatment. An obvious damage was evidenced to the tumor cells of mice by cell necrosis and apoptosis in the group of injection with $\text{Ag}_2\text{S}@Fe_2C\text{-DSPE-PEG-iRGD}$ and bevacizumab after laser irradiation. Mice treated with other groups showed less necrotic areas (Fig. 7E). These results showed that $\text{Ag}_2\text{S}@Fe_2C\text{-DSPE-PEG-iRGD}$ was an efficient nanozyme as targeting nanomaterials with antitumor capacity in 4T1 breast cancer-bearing mice.

Subsequently, toxicity analysis of these NPs was investigated in vivo. There was no decrease in the weight of the mice in each group during the treatment, which demonstrates the low toxicity of the $\text{Ag}_2\text{S}@Fe_2C\text{-DSPE-PEG-iRGD}$ (fig. S10C). The histological analysis was done by hematoxylin and eosin (H&E) staining of the main organs after the treatment to study the damage in acute and chronic stages. No tissue necrosis was observed in the main organs (heart, liver, spleen, lung, and kidney) for the seven groups (fig. S12), demonstrating that the $\text{Ag}_2\text{S}@Fe_2C\text{-DSPE-PEG-iRGD}$ have no significant side effects in vivo.

DISCUSSION

The complicated TME has brought great challenge to the therapeutic effect of nanomedicine for a long time. As mentioned above, it is almost impossible for specific nanoagents to penetrate the tumor through targeted effect to achieve effective accumulation and cell uptake and then excrete through metabolism after treatment. To overcome the multiple biological barriers during the drug delivery, nanomedicine should be rationally designed. In this work, a precise targeting NP-based nanozyme system ($\text{Ag}_2\text{S}@Fe_2C\text{-DSPE-PEG-iRGD}$) was developed for theranostics of breast cancer. At the cellular level, the nanozyme showed the efficient capacity of cell uptake and ROS production. In addition, this nanozyme has developed prominent luminescence in NIR-II and MRI contrast properties, which will be helpful to the visual tracking in vivo. As a result, the improved therapeutic effect was observed by the treatment of $\text{Ag}_2\text{S}@Fe_2C\text{-DSPE-PEG-iRGD}$ after combination with the tumor vascular normalization based on bevacizumab during the treatment in 4T1 breast cancer-bearing mice. Furthermore, ~90% of injected $\text{Ag}_2\text{S}@Fe_2C\text{-DSPE-PEG-iRGD}$ was excreted from the body in 14 days. This rapid, high-degree excretion could promote clinical translation of $\text{Ag}_2\text{S}@Fe_2C\text{-DSPE-PEG-iRGD}$. Hence, this study presents a new therapeutic

strategy by the cooperation between catalysis of smart nanozyme system and tumor vascular normalization for intensive combination therapy of breast cancer, which would accelerate exploitation and clinical translation of nanomedicine.

MATERIALS AND METHODS

Synthesis of monodisperse $\text{Ag}_2\text{S}@Fe_2C$ NPs

$\text{Ag}_2\text{S}@Fe_2C$ NPs were synthesized by a facile seed-mediated growth method. First, Ag_2S QDs were synthesized following our previously reported method. In the typical synthesis, Ag_2S QDs (10 mg liter⁻¹ in hexane, 1 ml), 1-octadecene (ODE) (62.5 mmol), NH_4Br (0.1 mmol), and Oleamine (OAm) (1 mmol) were mixed under a gentle N_2 flow for 30 min in a four-necked flask. Then, the solution was heated to 120°C and kept for 30 min to remove the organic impurities. $\text{Fe}(\text{CO})_5$ (5 mmol) was injected into the reaction system when the temperature reached 180°C and kept for 10 min, and the system was raised up to 300°C for another 30 min. After the system cooled down to room temperature, 27 ml of acetone was added to the system. After centrifugation, the product was washed by ethanol and hexane.

Synthesis of $\text{Ag}_2\text{S}@Fe_2C\text{-DSPE-PEG}$ and $\text{Ag}_2\text{S}@Fe_2C\text{-DSPE-PEG-iRGD}$

$\text{Ag}_2\text{S}@Fe_2C\text{-DSPE-PEG}$ was formulated using W/O emulsion method. Typically, DSPE-PEG- NH_2 (250.0 mg, 0.05 mmol) was dissolved in 12 ml of deionized water. Subsequently, $\text{Ag}_2\text{S}@Fe_2C$ NPs (10 mg ml⁻¹ in dichloromethane, 3 ml) was added to the system. Then, the mixed system was kept for 10 min by using ultrasound. The organic solvent in the obtained W/O emulsion was evaporated using a rotary evaporator at 25°C for 2 hours. $\text{Ag}_2\text{S}@Fe_2C\text{-DSPE-PEG}$ was obtained after centrifugation at 10,000g for 10 min. This synthesized $\text{Ag}_2\text{S}@Fe_2C\text{-DSPE-PEG}$ was dispersed in PBS buffer (pH 7.4) for further use. $\text{Ag}_2\text{S}@Fe_2C\text{-DSPE-PEG-iRGD}$ was synthesized by using the same method as $\text{Ag}_2\text{S}@Fe_2C\text{-DSPE-PEG}$; the only difference was the addition of DSPE-PEG-iRGD.

In vitro photothermal ablation of 4T1 cells

The cell LIVE/DEAD assays were also studied to investigate photothermal therapy in vitro. The 4T1 cells grown to 80% confluence in glass bottom 24-well plate were incubated with $\text{Ag}_2\text{S}@Fe_2C\text{-DSPE-PEG}$ for 4 hours, respectively. After washing the free NPs with Dulbecco's Phosphate-Buffered Saline (DPBS), fresh culture medium was added. Laser (808 nm, 0.3 W cm⁻²) was used to irradiate the adherent cell solution. After the Dulbecco's modified Eagle medium was removed, the cells were washed with PBS three times. Calcein-AM (100 μl) and PI solution (100 μl) were incubated with 4T1 cells for 15 min. Living cells were stained with calcein-AM (green fluorescence), and dead cells were stained with PI (red fluorescence) solution. The cells were then visualized using an inverted microscope (Olympus IX71) with a 10 \times under laser excitation at 475 and 542 nm.

In vivo antitumor efficiency evaluation

Mice bearing 200-mm³ 4T1 breast cancer were randomly divided into nine groups: (i) $\text{Ag}_2\text{S}@Fe_2C\text{-DSPE-PEG-iRGD}$, laser irradiation, and bevacizumab; (ii) $\text{Ag}_2\text{S}@Fe_2C\text{-DSPE-PEG-iRGD}$ and laser irradiation; (iii) $\text{Ag}_2\text{S}@Fe_2C\text{-DSPE-PEG}$, laser irradiation, and bevacizumab; (iv) $\text{Ag}_2\text{S}@Fe_2C\text{-DSPE-PEG-iRGD}$ and laser irradiation; (v) $\text{Ag}_2\text{S}@Fe_2C\text{-DSPE-PEG-iRGD}$; (vi) $\text{Ag}_2\text{S}@Fe_2C\text{-DSPE-PEG}$; (vii) bevacizumab;

(viii) laser irradiation only; and (ix) control (only saline). Nine mice were contained in each group. After 200 ml of saline or NPs (20 mg kg⁻¹) were intravenously injected into nude mice bearing the 4T1 breast cancer for 24 hours, mice were exposed to 808-nm laser (0.3 W cm⁻²) for 5 min and tail vein-injected with bevacizumab. The changes of body weight and tumor volume during 30 days of treatment period were recorded.

Histological evaluation

Immunohistochemical was stained using anti-CD31 antibody, according to the corresponding protocols. Mice from each group were euthanized; then, major organs and tumor were recovered, followed by fixing with 10% neutral-buffered formalin after 18-day treatment. The organs were embedded in paraffin and sectioned at 5 mm. H&E or Prussian blue staining was performed for histological examination. The slides were observed under an optical microscope.

Statistical analysis

All data are expressed as means ± SD. Statistical differences were determined by two-tailed Student's *t* test; **P* < 0.05, ***P* < 0.01, and ****P* < 0.001.

Ethical approval

All experiments involving animals were performed in accordance with the guidelines of the Institutional Animal Care and Use Committee of Peking University, Beijing, China.

SUPPLEMENTARY MATERIALS

Supplementary material for this article is available at <http://advances.sciencemag.org/cgi/content/full/6/48/eabc8733/DC1>

[View/request a protocol for this paper from Bio-protocol.](#)

REFERENCES AND NOTES

- N. Harbeck, F. Penault-Llorca, J. Cortes, M. Gnant, N. Houssami, P. Poortmans, K. Ruddy, J. Tsang, F. Cardoso, *Breast cancer. Nat. Rev. Dis. Primers*, **5**, 66 (2019).
- J. Liu, S. K. Lau, V. A. Varma, R. A. Moffitt, M. Caldwell, T. Liu, A. N. Young, J. A. Petros, A. O. Osunkoya, T. Krogstad, B. Leyland-Jones, M. D. Wang, S. Nie, Molecular mapping of tumor heterogeneity on clinical tissue specimens with multiplexed quantum dots. *ACS Nano* **4**, 2755–2765 (2010).
- Q. Liu, J. Cai, Y. Zheng, Y. Tan, Y. Wang, Z. Zhang, C. Zheng, Y. Zhao, C. Liu, Y. An, C. Jiang, L. Shi, C. Kang, Y. Liu, NanoRNP overcomes tumor heterogeneity in cancer treatment. *Nano Lett.* **19**, 7662–7672 (2019).
- D. Ling, W. Park, S.-j. Park, Y. Lu, K. Kim, M. J. Hackett, B. Kim, H. Yim, Y. Jeon, K. Na, T. Hyeon, Multifunctional tumor pH-sensitive self-assembled nanoparticles for bimodal imaging and treatment of resistant heterogeneous tumors. *J. Am. Chem. Soc.* **136**, 5647–5655 (2014).
- A. Sharma, M.-G. Lee, M. Won, S. Koo, J. F. Arambula, J. L. Sessler, S.-G. Chi, J. S. Kim, Targeting heterogeneous tumors using a multifunctional molecular prodrug. *J. Am. Chem. Soc.* **141**, 15611–15618 (2019).
- K. Melgar, M. M. Walker, L. M. Jones, L. C. Bolanos, K. Hueneman, M. Wunderlich, J.-K. Jiang, K. M. Wilson, X. Zhang, P. Sutter, A. Wang, X. Xu, K. Choi, G. Tawa, D. Lorimer, J. Abendroth, E. O'Brien, S. B. Hoyt, E. Berman, C. A. Famulare, J. C. Mulloy, R. L. Levine, J. P. Perentesis, C. J. Thomas, D. T. Starczynowski, Overcoming adaptive therapy resistance in AML by targeting immune response pathways. *Sci. Transl. Med.* **11**, eaaw8828 (2019).
- W. Fan, B. Yung, P. Huang, X. Chen, Nanotechnology for multimodal synergistic cancer therapy. *Chem. Rev.* **117**, 13566–13638 (2017).
- Y. Ma, Y. Zhang, X. Li, Y. Zhao, M. Li, W. Jiang, X. Tang, J. Dou, L. Lu, F. Wang, Y. Wang, Near-infrared II phototherapy induces deep tissue immunogenic cell death and potentiates cancer immunotherapy. *ACS Nano* **13**, 11967–11980 (2019).
- L. Wu, D. Leng, D. Cun, C. Foged, M. Yang, Advances in combination therapy of lung cancer: Rationales, delivery technologies and dosage regimens. *J. Control. Release* **260**, 78–91 (2017).
- R. van der Meel, E. Sulheim, Y. Shi, F. Kiessling, W. J. M. Mulder, T. Lammers, Smart cancer nanomedicine. *Nat. Nanotechnol.* **14**, 1007–1017 (2019).
- Y. Cao, J. Arbisser, R. J. D'Amato, P. A. D'Amore, D. E. Ingber, M. Klagsbrun, S. Lim, M. A. Moses, B. Zetter, H. Dvorak, R. Langer, Forty-year journey of angiogenesis translational research. *Sci. Transl. Med.* **3**, 114rv3 (2011).
- O. Takahashi, R. Komaki, P. D. Smith, J. M. Jürgensmeier, A. Ryan, B. N. Bekele, I. I. Wistuba, J. J. Jacoby, M. V. Korshunova, A. Biernacka, B. Erez, K. Hoshio, R. S. Herbst, M. S. O'Reilly, Combined MEK and VEGFR inhibition in orthotopic human lung cancer models results in enhanced inhibition of tumor angiogenesis, growth, and metastasis. *Clin. Cancer Res.* **18**, 1641–1654 (2012).
- J. M. L. Ebos, C. R. Lee, W. Cruz-Munoz, G. A. Bjarnason, J. G. Christensen, R. S. Kerbell, Accelerated metastasis after short-term treatment with a potent inhibitor of tumor angiogenesis. *Cancer Cell* **15**, 232–239 (2009).
- M. Páez-Ribes, E. Allen, J. Hudock, T. Takeda, H. Okuyama, F. Viñals, M. Inoue, G. Bergers, D. Hanahan, O. Casanovas, Antiangiogenic therapy elicits malignant progression of tumors to increased local invasion and distant metastasis. *Cancer Cell* **15**, 220–231 (2009).
- L. Tian, A. Goldstein, H. Wang, H. C. Lo, I. S. Kim, T. Welte, K. Sheng, L. E. Dobrolecki, X. Zhang, N. Putluri, T. L. Phung, S. A. Mani, F. Stossi, A. Sreekumar, M. A. Mancini, W. K. Decker, C. Zong, M. T. Lewis, X. H.-F. Zhang, Mutual regulation of tumor vessel normalization and immunostimulatory reprogramming. *Nature* **544**, 250–254 (2017).
- S. Huang, K. Shao, Y. Liu, Y. Kuang, J. Li, S. An, Y. Guo, H. Ma, C. Jiang, Tumor-targeting and microenvironment-responsive smart nanoparticles for combination therapy of antiangiogenesis and apoptosis. *ACS Nano* **7**, 2860–2871 (2013).
- L. Z. Gao, J. Zhuang, L. Nie, J. Zhang, Y. Zhang, N. Gu, T. Wang, J. Feng, D. Yang, S. Perrett, X. Yan, Intrinsic peroxidase-like activity of ferromagnetic nanoparticles. *Nat. Nanotechnol.* **2**, 577–583 (2007).
- H. Wei, E. K. Wang, Nanomaterials with enzyme-like characteristics (nanozymes): Next-generation artificial enzymes. *Chem. Soc. Rev.* **42**, 6060–6093 (2013).
- Y. Lin, J. Ren, X. Qu, Nano-gold as artificial enzymes: Hidden talents. *Adv. Mater.* **26**, 4200–4217 (2014).
- L. Z. Gao, X. Y. Yan, Nanozymes: An emerging field bridging nanotechnology and biology. *Sci. China Life Sci.* **59**, 400–402 (2016).
- X. Y. Wang, Y. H. Hu, H. Wei, Nanozymes in bionanotechnology: From sensing to therapeutics and beyond. *Inorg. Chem. Front.* **3**, 41–60 (2016).
- W. He, W. Warner, Q. Xia, J.-j. Yin, P. P. Fu, Enzyme-like activity of nanomaterials. *J. Environ. Sci. Health C* **32**, 186–211 (2014).
- Z. Tang, Y. Liu, M. He, W. Bu, Chemodynamic therapy: Tumour microenvironment-mediated Fenton and Fenton-like reactions. *Angew. Chem. Int. Ed.* **58**, 946–956 (2019).
- K. Fan, J. Xi, L. Fan, P. Wang, C. Zhu, Y. Tang, X. Xu, M. Liang, B. Jiang, X. Yan, L. Gao, In vivo guiding nitrogen-doped carbon nanozyme for tumor catalytic therapy. *Nat. Commun.* **9**, 1440 (2018).
- Y. Du, B. Xu, T. Fu, M. Cai, F. Li, Y. Zhang, Q. Wang, Near-infrared photoluminescent Ag₂S quantum dots from a single source precursor. *J. Am. Chem. Soc.* **132**, 1470–1471 (2010).
- Z. Yang, T. Zhao, X. Huang, X. Chu, T. Tang, Y. Ju, Q. Wang, Y. Hou, S. Gao, Modulating the phases of iron carbide nanoparticles: From a perspective of interfering with the carbon penetration of Fe@Fe₃O₄ by selectively adsorbed halide ions. *Chem. Sci.* **8**, 473–481 (2017).
- Y. Ju, H. Zhang, J. Yu, S. Tong, N. Tian, Z. Wang, X. Wang, X. Su, X. Chu, J. Lin, Y. Ding, G. Li, F. Sheng, Y. Hou, Monodisperse Au–Fe₂C Janus nanoparticles: An attractive multifunctional material for triple-modal imaging-guided tumor photothermal therapy. *ACS Nano* **11**, 9239–9248 (2017).
- L. Chen, S. Yu, H. Wang, J. Xu, C. Liu, W. H. Chong, H. Chen, General methodology of using oil-in-water and water-in-oil emulsions for colling nanofilaments. *J. Am. Chem. Soc.* **135**, 835–843 (2013).
- Y.-P. Sun, B. Zhou, Y. Lin, W. Wang, K. A. S. Fernando, P. Pathak, M. J. Meziani, B. A. Harruff, X. Wang, H. Wang, P. G. Luo, H. Yang, M. E. Kose, B. Chen, L. M. Veca, S.-Y. Xie, Quantum-sized carbon dots for bright and colorful photoluminescence. *J. Am. Chem. Soc.* **128**, 7756–7757 (2006).
- K. Avgoustakis, A. Beletsis, Z. Panagi, P. Klepetsanis, A. G. Karydas, D. S. Ithakissios, PLGA–mPEG nanoparticles of cisplatin: In vitro nanoparticle degradation, in vitro drug release and in vivo drug residence in blood properties. *J. Control. Release* **79**, 123–135 (2002).
- M. Semeniuk, Z. Yi, V. Poursorkhabi, J. Tjong, S. Jaffer, Z.-H. Lu, M. Sain, Future perspectives and review on organic carbon dots in electronic applications. *ACS Nano* **13**, 6224–6255 (2019).
- R. F. Egerton, M. J. Whelan, Electron energy loss spectra of diamond, graphite and amorphous carbon. *J. Electron. Spectros. Relat. Phenomena* **3**, 232–236 (1974).
- Y. Zhong, Z. Ma, F. Wang, X. Wang, Y. Yang, Y. Liu, X. Zhao, J. Li, H. Du, M. Zhang, Q. Cui, S. Zhu, Q. Sun, H. Wan, Y. Tian, Q. Liu, W. Wang, K. C. Garcia, H. Dai, In vivo molecular imaging for immunotherapy using ultra-bright near-infrared-II rare-earth nanoparticles. *Nat. Biotechnol.* **37**, 1322–1331 (2019).
- B. Du, M. Yu, J. Zheng, Transport and interactions of nanoparticles in the kidneys. *Nat. Rev. Mater.* **3**, 358–374 (2018).
- J. Kim, H. R. Cho, H. Jeon, D. Kim, C. Song, N. Lee, S. H. Choi, T. Hyeon, Continuous O₂-evolving MnFe₂O₄ nanoparticle-anchored mesoporous silica nanoparticles for efficient photodynamic therapy in hypoxic cancer. *J. Am. Chem. Soc.* **139**, 10992–10995 (2017).
- Z. Wang, Y. Ju, S. Tong, H. Zhang, J. Lin, B. Wang, Y. Hou, Au₃Cu tetrapod nanocrystals: Highly efficient and metabolizable multimodality imaging-guided NIR-II photothermal agents. *Nanoscale Horiz.* **3**, 624–631 (2018).

37. Z. Wang, Y. Ju, Z. Ali, H. Yin, F. Sheng, J. Lin, B. Wang, Y. Hou, Near-infrared light and tumor microenvironment dual responsive size-switchable nanocapsules for multimodal tumor theranostics. *Nat. Commun.* **10**, 4418 (2019).
38. Y. Yang, Q. Chen, S. Li, W. Ma, G. Yao, F. Ren, Z. Cai, P. Zhao, G. Liao, J. Xiong, Z. Yu, iRGD-mediated and enzyme-induced precise targeting and retention of gold nanoparticles for the enhanced imaging and treatment of breast cancer. *J. Biomed. Nanotechnol.* **14**, 1396–1408 (2018).
39. Y. Zhang, G. Hong, Y. Zhang, G. Chen, F. Li, H. Dai, Q. Wang, Ag₂S quantum dot: A bright and biocompatible fluorescent nanoprobe in the second near-infrared window. *ACS Nano* **6**, 3695–3702 (2012).

Acknowledgments

Funding: This work was supported by the Natural Science Foundation of Beijing Municipality (L72008), the National Natural Science Foundation of China (51672010, 81421004, 51631001, 51590882, and 51602285), the National Key R&D Program of China (2017YFA0206301 and 2016YFA0200102), the Key Laboratory of Biomedical Effects of Nanomaterials and Nanosafety, National Center for Nanoscience and Technology, Chinese Academy of Sciences

(NSKF201607), and China Postdoctoral Science Fund (2019M660315). **Author contributions:** Z.W. and Y.H. conceived and designed the experiments. Z.W., Z.L., Z.S., S.L., S.Z., S.W., Q.R., and F.S. performed the experiments. Z.W. and Y.H. analyzed the results. Z.W., Z.A., B.W., and Y.H. wrote and revised the manuscript. Z.W. and Y.H. supervised the entire project. **Competing interests:** The authors declare that they have no competing interests. **Data and materials availability:** All data needed to evaluate the conclusions in the paper are present in the paper and/or the Supplementary Materials. Additional data related to this paper may be requested from the authors.

Submitted 19 May 2020

Accepted 13 October 2020

Published 27 November 2020

10.1126/sciadv.abc8733

Citation: Z. Wang, Z. Li, Z. Sun, S. Wang, Z. Ali, S. Zhu, S. Liu, Q. Ren, F. Sheng, B. Wang, Y. Hou, Visualization nanozyme based on tumor microenvironment “unlocking” for intensive combination therapy of breast cancer. *Sci. Adv.* **6**, eabc8733 (2020).